

1 Digital Elevation Model (DEM) uncertainty
2 and hazard analysis using a geophysical flow
3 model

4 E. R. Stefanescu¹, M. Bursik², G. Cordoba³, K. Dalbey⁴, M.
5 Jones⁵, A.K. Patra¹, D.C. Pieri⁶, E.B. Pitman¹, and M.F.
6 Sheridan²

7 ¹Department of Mechanical and Aerospace Engineering,
8 University at Buffalo

9 ²Department of Geology, University at Buffalo

10 ³Universidad de Nariño, Colombia

11 ⁴Sandia National Laboratories, Albuquerque, NM

12 ⁵Center for Computational Research, University at Buffalo

13 ⁶Jet Propulsion Laboratory, Caltech, Pasadena, CA, 91109
14 USA

15 June 9, 2011

16 **Abstract**

17 This paper describes a new methodology to quantify the variation
18 in the output of a computational fluid dynamics model for block and
19 ash flows, when the digital elevation model (DEM) of the terrain and
20 other inputs are given as a range of possible values with a prescribed

uncertainty. Integrating these variations in the possible flows as a function of input uncertainties provides us well-defined information on the hazards probability at specific locations, i.e., a hazard map. Earlier work provided a methodology for assessing hazards based on variations in flow initiation and friction parameters. This paper extends this to include the effect of terrain error and uncertainty. Our results based on potential flows at Mammoth Mountain, California, and Galeras Volcano, Colombia, establish the soundness of the approach and the effect of including the uncertainty in DEMs on the construction of probabilistic hazard maps.

1 Introduction

Perhaps the most fundamental product created by field volcanologists to characterize the potential for destruction of a volcano is the hazards map. Often a reasonable hazards map can be made when the distribution of deposits of a given type are well-exposed, and easily dated and mapped. In general, however, difficult logistics or paucity of previous work may render understanding of a volcano’s history quite incomplete. Moreover, the depositional record on the flanks of a volcano cannot often be assumed to be very complete.

Several workers have thus explored the use of computational fluid dynamics (CFD) models to produce volcanic hazard maps for a variety of phenomena at a number of volcanoes [Murcia et al., 2010, Procter et al., 2010, Sheridan et al., 2010]. Hazard maps for ground-hugging flows that are constrained by the terrain, such as pyroclastic density currents and lava flows are often constructed using a digital representation of the terrain [Takahashi and Tsujimoto, 2000, Dalbey et al., 2008]. Usually these terrain representations are digital elevation models (DEMs). For this type of study, terrain elevation is rightly recognized as the most essential and fundamental of variables in geographic analysis [Atkinson, 2002]. In earlier work, [Dalbey et al., 2008] we introduced procedures for constructing hazard maps using ensembles of CFD

51 models (the TITAN2D code [Patra et al., 2005]) of such flows constructed by
52 establishing probability distributions of input uncertainties in flow initiation
53 (location and volumes) and sampling these. The important contribution of
54 DEM uncertainty to the variability of the flow outcomes was not included in
55 that work since there were no readily available procedures for doing so. This
56 work is focused on addressing this lacuna.

57 A digital representation of a terrain surface is an approximation of reality
58 and is often subject to significant error. The error is usually not known in
59 terms of both magnitude and spatial distribution. There are in fact large
60 uncertainties associated with the construction of DEMs. In [Wechsler and
61 Kroll, 2006] it was shown that DEMs contain errors derived from a variety of
62 sources: sampling, measurement and interpolation, and these errors cannot
63 always be well estimated. When such DEMs are used in *a posteriori* analysis
64 for instance in a CFD model of possible flows the errors propagate to the
65 predicted flow.

66 The most important part of DEM error propagation analysis is the ap-
67 propriate characterization of the error within the DEM itself, including infor-
68 mation about its distribution and spatial structure [Shortridge, 2001]. DEM
69 vendors generally provide users with a measure of vertical accuracy in the
70 form of the root mean squared error (RMSE) statistic. However many pa-
71 pers have reported on the limitations of a single value of accuracy, stressing
72 that DEM error is spatially variable and autocorrelated [Wechsler and Kroll,
73 2006, Darnell et al., 2008]. Also the magnitude of the DEM error is closely
74 related to the characteristics of the terrain surface. For example, slope will
75 influence interpolation procedures.

76 DEM error propagation analysis was introduced to the GIS community in
77 the early 1990s. In the work of Heuvelink et al. [1990], error propagation in
78 calculating slope and aspect was represented using Monte Carlo simulation
79 and Taylor series approximation. It was shown that standard deviations of
80 slope and aspect were higher than expected. The effect of error in the DEMs
81 on the erosion models was emphasized. A method used by Weng [2002] in

quantification of the uncertainty of DEMs was to create various DEMs using different interpolation methods and to examine the RMSE from the source map, sampling and measurement error, and the interpolation process. It was concluded that RMSE can be used as a general indicator of DEM uncertainty. In recent literature, DEM error without spatial autocorrelation was considered to be a worst-case scenario [Heuvelink et al., 1989, Van Niel et al., 2004, Oksanen, 2006], but no analysis based on terrain morphology and the effect of different DEMs was done. Wechsler and Kroll [2006] developed four different methods for representing the spatial dependence of error through random fields to assess the effect on topographic parameters of the DEM uncertainty. The study showed that uncertainty in the DEM is manifested at higher elevations in local steeper slopes, on both slope and elevation maps. Florinsky [1998] showed that the effect of DEM uncertainty on the accuracy of slope and aspect estimation cannot be determined by using data from topographic maps or field surveys, because accurate derivatives cannot be determined.

One key feature of spatial data is the autocorrelation of observations in space. Generally, spatial autocorrelation refers to the correlation between the same attribute at two locations. Observations in close spatial proximity tend to be more related than are observations at larger distance or separation. Errors in spatial data (such as incorrect elevation values assigned to a point) are spatially autocorrelated. The effect of correlated DEM error has been investigated in the literature [Fisher, 1991, Goodchild et al., 1992]. It was shown that not only is error spatially variable throughout a DEM, but within the elevation model the error value of an individual grid cell is related to the error in neighboring cells. Unfortunately, DEM providers do not include information regarding the spatial dependence or spatial relationship of errors.

Stochastic modeling uses stochastic conditional simulation to generate multiple equally likely representations of an actual terrain surface. Hunter and Goodchild [1997], Ehlschlaeger and Shortridge [1996] computed a normal distribution of maps or realizations to reproduce the spatial autocorrelation

113 encountered in the original error surface, filtered using a Gaussian convo-
114 lution filter, with kernel sizes derived from autocorrelation analysis of the
115 original error surfaces.

116 Various researchers have applied stochastic techniques to evaluate un-
117 certainty in DEM data. Ehlschlaeger and Shortridge [1996] stochastically
118 simulated error in a DEM to evaluate the impact of DEM uncertainty on
119 a least-cost-path application. Hunter and Goodchild [1997] investigated the
120 effect of simulated changes in elevation at different levels of spatial autocorre-
121 lation on slope and aspect calculations. Hebel and Purves [2008] produced
122 uncertainty surfaces to show the impact of DEM uncertainty on an ice sheet
123 model. Darnell et al. [2008] developed a fuzzy framework to examine the
124 probable and possible uncertainties in classifying landslide hazard.

125 The aim of this paper is to quantify the variation in the output of a com-
126 putational flow model for block and ash flows, when the model inputs, includ-
127 ing the elevation values represented in the DEM, are uncertain or given as a
128 range of possible values. Integrating these variations in the possible flows as
129 a function of input uncertainties provides us well-defined information on the
130 probability of hazard at specific locations, i.e., a hazard map [Dalbey et al.,
131 2008]. In particular, we focus on assessing the influence of DEM uncertain-
132 ties (along with uncertainties in initial size and location of the avalanche,
133 and the internal and bed friction angles). There is uncertainty in all of these
134 inputs, which can be represented using either field data or stochastic meth-
135 ods. The distribution or the range of the parameters can be obtained from
136 laboratory and field instruments for friction angles, and historical records
137 of flow frequency and magnitude for size of the initial failure. Stochastic
138 methods are used to assess the uncertainties in the DEMs: a perturbation of
139 the elevation based on the measured error model, and also an unconditional
140 stochastic simulation [Ehlschlaeger and Shortridge, 1996]. Both methods gen-
141 erate multiple likely representations of the actual terrain, while the second
142 one accounts for the spatial autocorrelation between elevation points. The
143 effect of DEM uncertainty and its impact on the model output is analyzed

144 by constructing a hazards map and performing a "probability analysis" for
 145 two volcanoes with different morphology: Galeras Volcano, Colombia, and
 146 Mammoth Mountain, CA, USA. We adapt here an approach based largely on
 147 the method of Ehlschlaeger and Shortridge [1996], which uses the difference
 148 between two independent DEMs to train a Gaussian model of error.

149 We review in the next sections the basic methodology for generating an
 150 ensemble of DEMs representative of the true DEM. Subsequent sections sum-
 151 marize the TITAN2D flow simulation tool and its use in a systematic hazard
 152 analysis. The hazards analysis tool itself uses ensembles of TITAN2D simu-
 153 lations to construct statistical surrogate models of flow outcomes at different
 154 locations as a function of model inputs, such as flow volume, resistance to
 155 flow as modeled by a Coulomb frictional law, etc. Sampling of these surro-
 156 gates leads to the construction of effective hazard maps that reflect the range
 157 of uncertainty in the model inputs.

158 2 Methodology

159 In previous work [Stefanescu et al., 2010], the effect of DEM variability on
 160 the output of TITAN2D was investigated by comparing the output (maxi-
 161 mum flow depth over the entire simulated time) from different DEMs of the
 162 same site. These DEMs were obtained from different techniques at different
 163 resolution. Two types of analysis were performed: a qualitative analysis and
 164 a statistical analysis. The qualitative analysis consisted of a comparison of
 165 the footprint of the flow, extended to a pixel based classification. The pixels
 166 were classified into inundated and non-inundated classes. For the statistical
 167 analysis we performed a Kolmogorov – Smirnov test to check if two output
 168 datasets differed significantly. The conclusion was that for moderate and
 169 smaller scale flows, use of different DEMs affects computation of accurate
 170 footprints of the flow.

171 This conclusion motivated us in examining the effect of DEM uncertainty
 172 by creating a model of the error and sampling it to create an ensemble of

173 possible terrains. The flow simulation is then run on every member of this
174 ensemble.

175 Naive, cell-by-cell approaches to treating DEM uncertainty quickly lead
176 to the use of thousands if not millions of random variables, resulting in a
177 computationally infeasible problem. On the other hand, the error model
178 described above can be parameterized with one or two random variables.
179 The parametrization methods are based on the assumption that the available
180 DEM is a representation of the terrain to which errors have been added
181 because of instrumental uncertainty. Therefore, the DEM can be assumed
182 to be one of an infinite number of elevation realizations.

183 **2.1 Method 1**

In this paper, we have available two "types" of DEMs of each mountain, which are used in creating DEM-to-DEM difference maps. Different realizations of the terrain were constructed by adding to one DEM – considered to represent the "true" elevation – a "random" perturbation. Since any two types of DEMs are obtained using different techniques, the difference between them can be added to that which is assumed to be the "true" DEM to give us a set of possible DEMs. Thus, the resulting realizations are consistent with the available set of DEMs. Randomness in the perturbations is created by multiplying the difference map with a normally distributed factor between 0 and 1.

$$R = M + \epsilon \cdot Diff \tag{1}$$

184 where R is a realization of the terrain, M is the DEM that best represents
185 the terrain (the "true" DEM), $Diff$ is the difference map and ϵ is a random
186 variable. In this way we can define a set of DEM realizations using only one
187 random variable.

2.2 Method 2

For elevation, data at any grid point in a DEM tends to be related to data from nearby points. This is the principal motivation of Method 2, based on the work of [Ehlschlaeger and Goodchild, 1994]. If more than one DEM exists for the same location, then difference maps can be constructed. Such maps are termed error maps. These maps are spatially autocorrelated. Random fields can be used to represent these spatially autocorrelated data points. Let $Z(\mathcal{U})$ be a continuous random field used to characterize unknown elevation errors (differences). The random field function we use is implemented in the function *r.random.surface* [Ehlschlaeger and Goodchild, 1994] of GRASS GIS [Mitasova et al., 1996], and generates fields obtained using a normal distribution (mean of 0.0 and variance of 1.0). The random field function derives its spatial dependence from the use of a distance based decay filter function. The following equation is used to generate the random field:

$$Z(\mathcal{U}) = \frac{\sum_v w_{u,v} \epsilon_v}{\sqrt{\sum_v w_{u,v}^2}}, \quad u \in \mathcal{U}, v \in \mathcal{V} \quad (2)$$

$$w_{u,v} = \begin{cases} 1 & : d_{u,v} \leq F \\ \left(1 - \frac{d_{u,v}-F}{D-F}\right)^E & : F < d_{u,v} \leq D, u \in \mathcal{U}, v \in \mathcal{V} \\ 0 & : d_{u,v} > D \end{cases} \quad (3)$$

where \mathcal{V} is the set of points potentially influencing points in a given area, \mathcal{U} , $w_{u,v}$ is the spatial autocorrelative effect between points $u \in \mathcal{U}$ and $v \in \mathcal{V}$, ϵ_v is a random variable with a mean of 0 and variance of 1, $d_{u,v}$ is the distance between u and v , D is the minimum distance of spatial independence, E is the distance decay exponent, and F the distance at which errors are completely correlated.

A set of random fields is calibrated to the spatial variation of the field being simulated using a correlogram function. We do this by fitting the correlogram and choosing the best descriptive parameters of the random

198 field (the minimum distance of spatial independence, the correlated distance
 199 decay exponent and the filter parameter) in a weighted least-square estimator
 200 implemented in GRASS's *r.lags.difference*. After running hundreds of tests
 201 with multiple combinations of D , E and F , we found the best random field to
 202 fit the error map characteristics based on the minimum sum of least squares
 203 difference between an error field's correlogram and the target correlogram.
 204 Figure 1 shows a sample error map correlogram and several trial correlograms
 205 closely fitting it. From Eqn 3 it can be seen that the parameters D , E and F
 206 influence the shape/look of the correlogram. We note that the main impact
 207 of the exponent value is to determining the roughness of the texture of the
 208 random surface. Texture roughness will decrease as the exponent value gets
 209 closer to 1.0. Once the parameters are set to a certain value as determined
 210 above we are able to sample from a normal distribution values for ϵ_v as given
 211 in Eqn 2 to generate a possible perturbation of the provided DEMs. In
 212 this way a normal distribution of possible terrain maps is produced where
 213 the mean of the distribution represents the original DEM used as the "true"
 214 surface.

The correlogram model was used with sequential Gaussian simulation to
 generate N error map realizations. Each error realization was added to the
 "true" DEM to generate equally probable realizations of the topography for
 the error structure of a DEM under consideration:

$$R(U) = m(U) + m(m(T)) + (m(s^2(T)) \cdot \epsilon) \cdot Z(U) \quad (4)$$

215 where $R(U)$ is a realization of an elevation dataset $m(U)$, T is a group of sets
 216 of spatially uncorrelated sample points, and ϵ is a random variable with mean
 217 0.0 and variance 1.0. The mean and the standard deviation are determined
 218 from randomly drawn, spatially independent points scattered across the error
 219 map. The error map was generated by subtracting the lower quality DEM
 220 from the "true" DEM, and characterizes the error of the lower quality DEM
 221 at each point.

2.3 DEM realizations

Many DEM users are aware that DEM uncertainty affects the results of their application, however, in most cases the DEM is accepted as the true representation of the earth’s surface. In this section, the two methods for generating multiple realizations of the terrain are presented for both Galeras Volcano and Mammoth Mountain, to test whether it is safe to assume that the representation of topography is acceptable as it is.

The motivation for creating realizations of the DEM was to be able to use the DEM along with other uncertain parameters as uncertain inputs for the calculation of a hazard map using the computational fluid dynamical model TITAN2D. One of our working hypotheses is that the DEM contributes a significant proportion of the variance in simulated flow, hence hazard map output. For sampling the input parameter space, a Latin Hypercube Sampling (LHS) was implemented.

For Galeras Volcano, two test DEMs at 30 m spacing were considered for our analysis. The SRTM (Shuttle Radar Topography Mission) 30m DEM was derived by spline interpolation from a 90m DEM of southern Colombia using radar data collected in 2000, while the ASTER (Advanced Spaceborne Thermal Emission and Reflection Radiometer) DEM was calculated at the Jet Propulsion Laboratory using orthorectified imagery from 12 January 2010 (Fig. 2 a). The ASTER dataset was used as a surrogate for the “true” elevation while the SRTM dataset was used in creating the error model.

Two 30-m resolution DEMs derived from independent techniques were used for Mammoth Mountain. A TOPSAR dataset was considered to be the “true” elevation, while an SRTM dataset was used in creating the error map. A rectangular area of approximately 42 kilometers² was defined within the TOPSAR and SRTM DEMs (Fig. 2 b).

For Method 1, sixty-four (64) DEM realizations were created and used as input parameters for the TITAN2D simulator along with uncertain parameters presented in 3.3. The input space is defined by seven parameters.

As described above for Method 2, realizations of the terrain surface were

253 created by taking into consideration the spatial autocorrelation of the error.
 254 The error map was obtained by subtracting the elevation of a given DEM
 255 from the “true” elevation at each location. The correlogram for the difference
 256 map was calculated to determine the range of spatial dependence of eleva-
 257 tion points. We found that spatial dependence persisted above a threshold
 258 value of the correlogram cross-correlation coefficient of 0.4 to a distance of
 259 2500 meters for Galeras and 2100 meters for Mammoth. To determine the
 260 probability distribution function (pdf) for the stochastic simulation, 91 sets
 261 of spot locations were selected from the map, each set containing 91 points,
 262 all pairs of points were separated by more than 2500 meters or 2100 meters,
 263 respectively. For each DEM, pdf statistics were derived. The random field
 264 parameters were chosen after testing more than 400 random field parameters
 265 for the smallest difference between the error model correlogram and the ran-
 266 dom field. This occurs when the minimum distance of spatial independence,
 267 $D = 2500$; the distance decay, $E = 0.8$, and the filter parameter, $F = 400$
 268 for Galeras and $D = 2100$, $E = 0.7$, and $F = 350$ for Mammoth. A total
 269 of 64 equally probable potential elevation surfaces of the area having a 30-m
 270 resolution were generated.

271 **2.4 Hazard map construction**

272 There are numerous ways to create a volcanic hazard map based on com-
 273 putational fluid dynamics modeling. The traditional Monte Carlo method
 274 can be used if we assume that uncertainty in model input parameters is the
 275 main restriction to our knowledge of future events at a given volcano. This
 276 is the case, for example, if we know that block and ash flows are common
 277 at a given volcano, but it is difficult to know the size or volume of potential
 278 future events. Although Monte Carlo is relatively simple to implement, it
 279 converges slowly and is unaffordable computationally because of the number
 280 of time-consuming simulations. A single TITAN2D run might take 20 min-
 281 utes on a single processor. To obtain three-digit accuracy in the expected
 282 value of a specified function would require a million runs. One million runs

283 of 20-min calculations running non-stop on 64 processor would take 217 days
284 [Dalbey et al., 2008].

285 Here, we briefly described the use of an hierarchical emulator that signif-
286 icantly reduces computational cost; a detailed discussion of the methodology
287 can be found in Dalbey [2009], Dalbey et al. [2008]. An emulator can be
288 thought of as a fast surrogate for a single numerical model simulation (a sim-
289 ulator). We describe the process of computing a hazard map for block and
290 ash flows with uncertain model inputs introduced by Dalbey [2009]. Two-
291 level construction of a group or ensemble of emulators is used to include
292 a separation of uncertain inputs and geographic coordinates. The process
293 starts by identifying the model inputs whose uncertainties will drive the pro-
294 cess. In our case, the uncertain flow inputs we use are volume and shape,
295 starting location, basal and internal friction angles, and finally topography,
296 as given by the DEM. For the resulting eight-dimensional parameter input
297 space, a Latin Hypercube Sampling was performed to determine parameter
298 values at which simulations were to be run [Mitasova et al., 1996]. As pri-
299 ors for the emulator, simulation outputs for each of these input parameter
300 vectors were stored at 64 grid points.

301 The output variable of interest for our application is the field of maximum
302 flow depth over time for each spatial position, at each of the downsampled
303 input parameter gridpoints. Tessellations of the geographic coordinate space
304 and the parameter input space are constructed (we use Delaunay triangu-
305 lation). At a designated location, \mathbf{x}^* , of the input parameter plus spatial
306 coordinate space at which the hazard is to be computed, the covering sim-
307 plex $S_{\mathbf{x}}^*$ of the parameter space is identified, and all nodes of that simplex
308 are enumerated, as are all nodes within a neighborhood (two hops in the
309 tessellation) of the covering simplex nodes. For each such two-hop node, we
310 tessellate in the spatial coordinates and evaluate all emulators constructed
311 over these nodes. We average these coordinate space emulators to (the coor-
312 dinate components of) \mathbf{x}^* by barycentric weighting; notice there will be an
313 emulator for each parameter input sample point. Now in the input parameter

space, construct a tessellation of the two-hop nodes and average the emulators to \mathbf{x}^* by barycentric weighting of the fine-scale emulator. The emulator is now readily and quickly evaluated for each evaluation. The hazard map construction can now proceed by treating the emulator as a surrogate for the simulator in the classical Monte Carlo procedure. For any point in the domain we can now exercise the emulator to get potential flows and hence exceedance probabilities.

2.5 TITAN2D and flow simulations

TITAN2D was developed for modeling dry geophysical granular flows, such as debris avalanches and block and ash flows. Given a digital elevation map specifying the topography of a volcano and the values of input parameters, including the initial volume of erupted material and the friction angles, TITAN2D calculates the flow depth and velocity at any location throughout the duration of an event. The TITAN2D code combines numerical simulations of a natural granular flow with digital terrain data. It is based on a depth-averaged model for an incompressible granular material governed by Coulomb-type friction interactions [Savage and Hutter, 1989]. The governing equations are obtained by applying conservation laws to the incompressible continuum, providing appropriate constitutive modeling assumptions, and then taking advantage of the shallowness of the flows (flows are much longer and wider than they are deep) to obtain simpler depth-averaged representations [Patra et al., 2005]. The motion of the material is considered to be gravitationally driven and resisted by both internal and bed friction. The stress boundary conditions are: no stress at the upper free-surface and a Coulomb-like friction law imposed at the interface between the material and the basal surface.

The primary factor driving the flow is the component of gravity tangential to the surface, which depends on a local slope computed from the elevation data, hence, the criticality of the DEM to the flow computations. The resulting hyperbolic system of equations was solved using a finite-volume scheme

344 with a second-order Godunov solver. Although many real geophysical flows
345 — such as debris flows — are fluidized, in this study we deal only with gran-
346 ular material that has not been fluidized, such as dome-collapse block and
347 ash flows or rock avalanches initiated by slope instability. The program runs
348 in parallel, using the Message Passing Interface (MPI) to allow communica-
349 tion between multiple processors, increasing computational power, decreasing
350 computational time and allowing use of large datasets. The algorithm uses
351 local adaptive mesh refinement for shock capturing, and dynamic load bal-
352 ancing for the efficient use of computational resources. Topographic data
353 are included in the simulation through a preprocessing routine in which the
354 digital elevation data are imported. TITAN2D performs flow simulations on
355 a DEM of a desired region, the simulation accuracy being highly dependent
356 on the level of the DEM resolution and quality.

357 Inputs to the code are the size and location of the initial volume, the
358 internal and bed friction and the DEM. Dalbey et al. [2008] presented sev-
359 eral methods for characterizing the effect of input data uncertainty on model
360 output. At that time, efficient methods for representing the uncertainty
361 associated with spatial parameters like terrain elevation were not well under-
362 stood.

363 **2.6 Bayes Linear Method**

364 The straightforward way to account for uncertain inputs and stochastic forc-
365 ing is a Monte Carlo approach — run many simulations and ‘average’ the
366 results in some fashion. If simulations are expensive to run, this approach
367 is not feasible. To circumvent this difficulty, the statistics community has
368 developed the idea of an emulator. In essence, the emulator is a regression
369 surface based on a representative sample of simulations at selected inputs,
370 accompanied by statistical error bounds. Equipped with this surface, output
371 values at new (untested) input values need not be run. Instead output re-
372 sults can be determined by evaluating the emulator. There are indeed many
373 methods – kriging, metamodels, support vector machines, etc., by which such

374 surrogates may be constructed and there exists a body of literature on the
 375 topic [Simpson et al., 2001, Clarke et al., 2005]. One often-used emulator is
 376 the GAuSSian Process (GASP) emulator, which assumes the regression has
 377 the form of a trend plus a Gaussian [Kennedy and O’Hagan, 2001, Conti
 378 and O’Hagan, 2007, O’Hagan, 2006, Bayarri et al., 2010]. To construct a
 379 GASP emulator, the covariance structure of the Gaussian must be assumed
 380 and parameters determined by Bayesian or partially Bayesian methodology.
 381 A fully Bayesian determination of the emulator can be costly, especially if
 382 the input data is high-dimensional. Here we use the Bayes Linear method
 383 (BLM) [Goldstein, 2007] to construct an emulator. Given prior beliefs (B) of
 384 mean and variance, the BLM updates these beliefs conditioned on the data
 385 (D). Note that “data” generally here refers to the output of computationally
 386 expensive physics based simulators. Because only the first two moments of
 387 a distribution are determined, the BLM is exact only for Gaussian distribu-
 388 tions. As an emulator construction, the BLM update is simpler than a full
 389 GASP construction, but the resulting emulator is comparable. Given the
 390 prior expectation $E[B]$ and variance $var(B)$, the BLM updates are

$$\begin{aligned}
 E_D(B) &= E[B] + cov(B, D)(var(D))^{-1}[D - E[D]] \\
 var_D(B) &= var(B) - cov(B, D)(var(D))^{-1}cov(D, B)
 \end{aligned}
 \tag{5}$$

391 These update formulae can be derived by minimizing the mean square error
 392 $(B - a^T D)^2$ between B and some linear combination of the data. Thus the
 393 BLM update can be viewed as the projection of the set of prior beliefs onto
 394 the span of the data.

395 **3 Implementation**

396 **3.1 Case study I: Galeras Volcano**

397 Galeras Volcano (elevation 4,276 meters), located in southwestern Colombia
 398 ($1^\circ 13.31'$ N and $77^\circ 21.68'$ W), is one of the most active volcanoes on the

399 world [Hurtado and Cortes, 1997]. Nearly 400,000 people currently live near
400 the volcano; 10,000 of them reside within the zone of high volcanic hazard.
401 Pyroclastic flows pose a major hazard for this population. The current period
402 of activity that began in 2004 presents a serious problem for all stakeholders:
403 decision makers, scientists, public safety officials, and the general population.
404 Computational modeling has the potential to provide useful information for
405 hazard assessment and risk mitigation. However, there is a need to evaluate
406 the validity of the modeling and the quality of the DEMs available for use in
407 such modeling.

408 Galeras is an important volcano for computational flow modeling from
409 both risk management and scientific perspectives [Calvache et al., 1997].
410 Forecasts of volcanic explosions using various geophysical tools [Narvaez
411 et al., 1997] have occasionally brought public warnings to a high level of
412 alert during the past 20 years. When the alert reaches the highest level,
413 the public are urged to evacuate some local areas; this occurred as recently
414 as January, 2010. The worst event at Galeras occurred in 1993, when an
415 eruption killed 9 scientists and journalists [Baxter and Gresham, 1997].

416 The topography of the volcano presents a problem for creation of a good
417 DEM. The irregular morphology on a small scale, with steep slopes, narrow
418 channels, deep gorges and abrupt cliffs poses problems for the creation of
419 accurate topographic models [Ordoñez Villota and Jentzsch, 2000]. In addition,
420 the current flow hazard map at Galeras is mainly based on the sparse
421 geological record [Calvache, 1990]. Dense vegetation, deep erosion, successive
422 deposits of lava and pyroclastic flows hinder the tracing of specific deposits in
423 the field. The diverse effects of this landscape, as reflected in DEMs created
424 by different processes and of different scales, must be examined and quantified
425 to determine the level of confidence that can be placed in model results.
426 Galeras provides a wide range of topographic features that challenge the use
427 of computational flow models.

428 **3.2 Case study II : Mammoth Mountain**

429 Mammoth Mountain is a large, geologically young, composite dome volcano
430 located on the southwestern rim of Long Valley Caldera, California [Bailey,
431 1989]. There are many active hazards issues for Mammoth Mountain, in-
432 cluding snow avalanches, rock avalanches and debris flows. In addition, it is
433 intersected by the Mono-Inyo Craters volcanic chain, which is the most active
434 volcanic region in the southwestern U.S. If Mono-Inyo type activity occurs
435 on Mammoth Mountain, then domes may form. These new domes would
436 be growing atop a steep edifice, and therefore could become gravitationally
437 unstable. Given that block and ash flows occurred at Mammoth Mountain
438 during its older dome growth stage, there is reason to believe that renewed
439 dome formation would result in block and ash flow activity. If this is so, then
440 parts of Mammoth Lakes, CA, are at risk from block and ash flows. Our
441 previous work on Mammoth Mountain (Stefanescu et al., submitted) was
442 the testing of the hypothesis that different DEMs result in different model
443 outputs of block and ash flow inundation.

444 **3.3 Model Set-up**

445 In our process to quantify the DEM uncertainties using TITAN2D, a set of
446 parameters was drawn on which to set the bounds of the input domain: in-
447 ternal friction angle, basal friction angle, flow volume, location and DEM.
448 The numerical values for these parameters were chosen to bracket the range
449 of flow volumes and initial locations, and to be representative of the friction
450 angles that have been used by other researchers in their computational mod-
451 els. The same reasonable parameter values were used for both volcanoes,
452 so they do not necessarily represent any optimization for a particular case.
453 The internal friction angle has little effect on the output of the flow models
454 [Dalbey et al., 2008, Sheridan et al., 2005]. Many TITAN users have chosen
455 values of internal friction that range between 15 and 37 degrees with values
456 between 30 and 35 being the most frequent values used [Patra et al., 2005,

457 Murcia et al., 2010]. For our study we use an internal friction angle uniformly
458 distributed between 20 and 25 degrees.

459 The value of the basal friction angle has a large effect on flow dynamics in
460 the TITAN2D simulations [Patra et al., 2005, Stinton et al., 2006]. Factors
461 that could affect the choice of basal friction angle include the volume of the
462 flow, the type of the pyroclastic flow, the nature of the substrate and the
463 amount of channelization. Murcia et al. [2010] listed the basal friction values
464 chosen by TITAN2D users; they range between 5 and 28 degrees; the mean
465 value being about 15 degrees. We are using a basal friction angle uniformly
466 distributed between 15 and 20 degrees.

467 Volumes of pyroclastic flows at stratovolcanoes typically cover a few or-
468 ders of magnitude. The volume values in this study bracket the range of
469 possible pyroclastic flows for both Mammoth and Galeras. According to
470 Calvache [1990], Galeras volcano produced 5 large pyroclastic flow eruptive
471 episodes; an historic eruption in 1866, and prehistoric events in 1100, 2300,
472 2900, and 4500 yBP. The total deposit volumes of these episodes range from
473 $O(10^6 - 9 \times 10^6)m^3$. Block and ash flows on Mammoth Mountain might
474 contain $O(10^5 - 10^7)m^3$ of material [Patra et al., 2005, Burkett, 2007]. Thus,
475 our choice of volumes ranges from 1.9×10^5 to $5 \times 10^6 m^3$. The shape of the
476 initial failure region is approximated as a paraboloid for which the volume
477 is calculated as $V = \frac{\pi}{2} \cdot r_{min} \cdot r_{max} \cdot h_{max}$. For a good match of the volume
478 range, the radius values were uniformly distributed between 25 and 500 m,
479 while the initial height followed the same distribution with values between
480 10 and 150 m.

481 Initiation locations were taken from previous mapping of vent sites, cou-
482 pled with knowledge of known weak areas within the volcano as indicated
483 by hydrothermal alteration. Around the centers of the separate initiation
484 locations, different starting positions were uniformly distributed in a circle
485 of radius 200 m. A rectangular area of approximative $40 km^2$ was defined
486 around the vent within the available DEMs as the potential run-out area.

487 4 Results and Conclusions

488 One of the goals of our analysis was to understand the effect of the spatial
 489 structure of available DEMs on hazard maps. Figure 2 (c) and (d) show the
 490 correlograms for the ASTER DEM and the TOPSAR DEM, which are the
 491 DEMs considered to best represent the real topography for Galeras Volcano
 492 and Mammoth Mountain, respectively. It is apparent that data processing
 493 resulted in a smoothing and filtering of the TOPSAR DEM which causes
 494 the correlation coefficient to vary smoothly as a function of distance and any
 495 two elevation values. Using a distance between two points of 2000m, for the
 496 ASTER DEM the correlation coefficient is 0.6, whereas for the TOPSAR
 497 DEM the correlation coefficient is 0.4. This means that elevation values
 498 within the ASTER DEM are more highly correlated.

499 Starting from these premises, we can explain the hazard map output for
 500 the cases when the DEM is considered to be an input parameter for the
 501 TITAND2D model. Figures 3 (a) and (c) display maps of Galeras of the
 502 probability that the flow depth will exceed 0.5 m in the next ten years using
 503 Method 1 or Method 2, respectively, to create the terrain realizations.

504 Figures 3 and 4 show maps at Galeras and Mammoth of the spatially
 505 varying lack of confidence in the probability hazard map depicted in Figure 4
 506 (a) and (b), respectively. The lack of confidence is defined as the computed
 507 standard deviation of hazard probability σ_P divided by the hazard proba-
 508 bility, P . When calculated by standard means, as was done here, the ratio
 509 σ_P/P measures the lack of confidence in the statistic, P , due to insufficient
 510 re-sampling of the input parameter space.

511 After a visual inspection of the figures we can conclude that the difference
 512 between hazard map outputs is more obvious for Galeras than for Mammoth
 513 Mountain. From the lack of confidence figure it is observed that in both cases
 514 the error is concentrated at flow margins.

515 For Mammoth Mountain the differences are less obvious, but with impor-
 516 tant differences again concentrated at the edge of the flow. An illustration of
 517 how the probabilities vary for Method 1 compared to Method 2 is shown in

Figure 5. We observe in comparing every point where there is a probability of having a flow depth greater than 0.5 m, the results for Galeras show a greater dispersion than do those for Mountain Mountain. When the flow is deep, the probability is high and tends to cluster near unity for both mountains. As the probability decreases, dispersion becomes greater for Galeras. We can conclude that as the error map becomes more highly correlated, one should use a more complex method for creation of topographic realizations such as stochastic Method 2. It appears that the spatial autocorrelation of the elevation points influences the hazard map output and a random perturbation of the elevation such as that used in Method 1 will not capture this effect.

One of the conclusions of our previous work was that for moderate and smaller-sized flows, different representations of the terrain more profoundly affect computation of an accurate flow footprint. For the present contribution, we have built a new set of hazard maps for the case when the volume is low, with a range between $10^4 - 5 \times 10^4 \text{ m}^3$ and for a high volume between $9 \times 10^6 - 5 \times 10^7 \text{ m}^3$. Since only 517 spatial cells for Mammoth and 872 cells for Galeras were included in the flow footprint for the low-volume case, for any particular cell, the probability that the flow would include that cell tends toward unity (in the case of cells within the starting region), or zero (in the case of any cell outside of the starting region but still within the footprint). Thus the probability plot appears nearly binary, which means that we have a hazard (flow greater than 0.5m) with either probability ~ 1 or ~ 0 Figure 6 (a), (b). We observe that there is a significant mismatch of prediction between the two methods (left upper corner and right lower corner in both figures) for both volcanoes that can be critical in the case of a hazards or risk assessment. For high-volume flows at Galeras, we observe that the area of probability greater than zero is much smaller when we are using Method 2 (topography is correlated) compared to Method 1 (no correlation of error between topographic points). We do not know the reason for this counterintuitive effect.

549 Our main goal was to explore the effect of DEM uncertainty in construct-
550 ing a hazards map. A quantitative and qualitative analysis is performed
551 for the case wherein the “original” or “best” deterministic DEM (ASTER
552 30m for Galeras and TOPSAR 30m for Mammoth as in Figure 7) is used as
553 input parameter for the hierarchical emulator, the output of which is then
554 contrasted with the case wherein the input is a set of terrain realizations.

555 We thus compare the hazard maps produced when DEM uncertainty is
556 not included against maps produced when DEM uncertainty is included. Fig-
557 ures 8 and 9 show that for Galeras the probability that the flow was deeper
558 than 0.5m varies considerably from the case of no DEM uncertainty. Hence,
559 the DEM is an important input parameter of which the errors need to be
560 carefully considered in flow modeling, and the effect of the DEM is not dimin-
561 ished by other uncertain parameters or the methodology used. We observe
562 that the uncertainty of having flow greater than 0.5 m increases towards the
563 flow edge. For Mammoth Mountain, the DEM uncertainty results in more
564 uncertainty in the flow outline when Method 2 is used. One of the causes
565 might be that the flow propagates a shorter distance compared to that in the
566 original DEM.

567 Because the uncertainty in flow outline increases for the case of Galeras,
568 where the autocorrelation is higher, we can furthermore say that perturbing
569 the DEM is more important as autocorrelation increases.

570 **Acknowledgments.** This work was supported by NASA grant NNX08AF75G.
571 The work and opinions expressed herein are those of the authors alone and do
572 not reflect the opinion of NASA. We are grateful to JPL for the construction
573 and distribution of the TOPSAR dataset.

574 References

575 P.M. Atkinson. Surface modelling: What’s the point? *Transactions in GIS*,
576 6:1–4, 2002.

577 R.A. Bailey. *Geologic Map of Long Valley Caldera, Mono-Inyo Craters Vol-*
578 *canic Chain and Vicinity, Eastern California*. Department of the Interior,
579 Reston, VA (US), 1989.

580 P.J. Baxter and A. Gresham. Deaths and injuries in the eruption of Galeras
581 Volcano, Colombia, 14 January 1993. *Journal of Volcanology and Geother-*
582 *mal Research*, 77:325–338, 1997.

583 M.J. Bayarri, J.O. Berger, E. Calder, K. Dalbey, S. Lunagomez, A.K. Patra,
584 E.B. Pitman, E.T. Spiller, and R.L. Wolper. Using statistical and computer
585 models to quantify volcanic hazards. *to appear Technometrics*, 2010.

586 S.M. Burkett. Geomorphic mapping and petrography of mammoth mountain,
587 california. Master’s thesis, State University of New York at Buffalo, 2007.

588 M. Calvache. Geology and volcanology of the recent evolution of Galeras
589 Volcano, Colombia. *Msc. Thesis. Louisiana State University*, page 171,
590 1990.

591 M. Calvache, G.P. Cortes, and S.N. Williams. Stratigraphy and chronology
592 of the Galeras volcanic complex, Colombia. *Journal of Volcanology and*
593 *Geothermal Research*, 77:5–19, 1997.

594 S.M. Clarke, J.H. Griebisch, and T.W. Simpson. Analysis of support vector
595 regression for approximation of complex engineering analyses. *Journal of*
596 *Mechanical Design*, 127(6):1077–1088, 2005. doi: 10.1115/1.1897403.

597 S. Conti and A. O’Hagan. Bayesian emulation of complex multi-output and
598 dynamic computer models. *Research Report No. 569/07, Department of*
599 *Probability and Statistics, University of Sheffield. Submitted to Journal of*
600 *Statistical Planning and Inference*, 2007.

601 K. Dalbey. Predictive simulation and model based hazard maps of geophys-
602 ical mass flows. *PhD thesis, Department of Mechanical and Aerospace*
603 *Engineering, University at Buffalo*, 2009.

- 604 K. Dalbey, A.K. Patra, E.B. Pitman, M.I. Bursik, and M.F. Sheridan. In-
 605 put uncertainty propagation methods and hazard mapping of geophys-
 606 ical mass flow. *Journal of Geophysical Research*, 113:5203–5219, 2008.
 607 doi:10.1029/2006JB004471.
- 608 A.R. Darnell, N.J. Tate, and C. Brunsdon. Improving user assessment of
 609 error implications in digital elevation models. *Computers, Environment
 610 and Urban Systems*, 32:268–277, 2008.
- 611 C. Ehlschlaeger and M.F. Goodchild. Uncertainty in spatial data: Defining,
 612 visualizing, and managing data errors. In *Proceedings GIS/LIS’94*, pages
 613 246–253, 1994.
- 614 C. Ehlschlaeger and A. Shortridge. Modeling elevation uncertainty in ge-
 615 ographical analysis. In *Proceedings of the International Symposium on
 616 Spatial Data Handling, Delf, Netherlands*, pages 9B.15–9B.25, 1996.
- 617 P.F. Fisher. Modeling soil map-unit inclusions by Monte Carlo simulation. *In-
 618 ternational Journal of Geographical Information Systems*, 5:193–208, 1991.
- 619 I.V. Florinsky. Accuracy of local topographic variables derived from digi-
 620 tal elevation models. *International Journal of Geographical Information
 621 Science*, 12:1:47–61, 1998.
- 622 M. Goldstein. Bayes linear methods I adjusting beliefs: Concepts and prop-
 623 erties. *Part 1 of 3 of online tutorial, website:*, 2007.
- 624 M.F. Goodchild, G. Sun, and S. Yang. Development and test of an error
 625 model for categorical data. *International Journal of Geographical Infor-
 626 mational Systems*, 6:87–104, 1992.
- 627 F. Hebelier and R.S. Purves. *Modelling DEM data uncertainties for Monte
 628 Carlo Simulations of Ice Sheet Models*, chapter Quality Aspects in spatial
 629 Data Mining, pages 175–196. A.Stein, J.Shi & W.Bijker, CRC Press, Boca
 630 Raton, 2008.

- 631 G.B.M. Heuvelink, P.A. Burrough, and H. Leenaers. Propagation of errors
632 in spatial modelling with GIS. *International Journal of Geographical In-*
633 *formation Systems*, 3:4(303-322), 1989.
- 634 G.B.M. Heuvelink, P.A. Burrough, and H. Leenaers. Error propagation in
635 spatial modelling with GIS. In *EGIS90 Proceedings - First European Con-*
636 *ference on Geographical Information Systems (EGIS Foundation: Utrecht,*
637 *The Netherlands)*, pages 453–462, 1990. In Harts J, HFL Ottens & HJ
638 Scholten (eds.).
- 639 G.J. Hunter and M.F. Goodchild. Modeling the uncertainty of slope and
640 aspect estimates derived from spatial databases. *Geographical Analysis*, 1:
641 35–49, 1997.
- 642 A. Hurtado and G.P. Cortes. Third version of the hazard map of Galeras
643 Volcano, Colombia. *Journal of Volcanology and Geothermal Research*, 77:
644 89–100, 1997.
- 645 M.C. Kennedy and A. O’Hagan. Bayesian calibration of computer models.
646 *Journal of the Royal Statistical Society: Series B (Statistical Methodology)*,
647 63(3):425–464, 2001.
- 648 H. Mitasova, J. Hofierka, M. Zlocha, and L.R. Iverson. Modeling topographic
649 potential for erosion and deposition using GIS. *International Journal of*
650 *Geographical Information Systems*, 10:629–641, 1996.
- 651 H.F. Murcia, M.F. Sheridan, J.L. Macias, and G.P. Cortes. TITAN2D sim-
652 ulations of pyroclastic flows at Cerro Machin Volcano, Colombia: Hazard
653 implications. *Journal of South American Earth Sciences*, 29:161–170, 2010.
- 654 L. Narvaez, R. Torres, D. Gomez, G.P. Cortes, H. Cepeda, and J. Stix.
655 Tornillo-type seismic signals at Galeras volcano, Colombia, 1992–1993.
656 *Journal of Volcanology and Geothermal Research*, 77:159–171, 1997.
- 657 A. O’Hagan. Bayesian analysis of computer code outputs: A tutorial. *Reli-*
658 *ability Engineering and System Safety*, 91(10-11):1290–1300, 2006.

- 659 J. Oksanen. *Digital Elevation Model error in terrain analysis*. PhD thesis,
660 Faculty of Science, University of Helsinki, 2006.
- 661 M. Ordoñez Villota and G. Jentzsch. Mediciones GPS como topografía ba-
662 sica para el estudio de microgravedad en el Volcán Galeras, Colombia.
663 *Ingeominas Internal Report (in Spanish)*, 2000.
- 664 A.K. Patra, A.C. Bauer, C. Nichita, E.B. Pitman, M. F. Sheridan, M. Bursik,
665 B. Rupp, A. Webber, L. Namikawa, and C. Renschler. Parallel adaptive
666 numerical simulation of dry avalanches over natural terrain. *Journal of*
667 *Volcanology and Geothermal Research*, 139:1–21, 2005.
- 668 J.N. Procter, S.J. Cronin, I.C. Fuller, M.F. M. Sheridan, V.E. Neall, and
669 H. Keys. Lahar hazard assessment using titan2d for an alluvial fan with
670 rapidly changing geomorphology: Whangaehu river, mt. ruapehu. *Geo-*
671 *morphology*, 116(1-2):162–174, 2010.
- 672 S.B. Savage and K. Hutter. The motion of a finite mass of granular material
673 down a rough incline. *Journal of Fluid Mechanics*, 199:177–215, 1989.
- 674 M.F. Sheridan, A.J. Stinton, A. Patra, E.B. Pitman, A. Bauer, and C.C.
675 Nichita. Evaluating TITAN2D mass-flow model using the 1963 Little
676 Tahoma Peak avalanches, Mount Rainier, Washington. *Journal of Vol-*
677 *canology and Geothermal Research*, 139:275–308, 2005.
- 678 M.F. Sheridan, A.K. Patra, K. Dalbey, and B Hubbard. Probabilistic digital
679 hazard maps for avalanches and massive pyroclastic flows using titan2d. *in*
680 *Groppelli G. and Viereck-Goette, L., editors, Stratigraphy and Geology of*
681 *Volcanic Areas , Geological Society of America Special Paper*, 464:281–291,
682 2010.
- 683 A. Shortridge. Characterizing uncertainty in digital elevation models. *Spatial*
684 *Uncertainty in Ecology: Implications for Remote Sensing and GIS Appli-*
685 *cations (Springer: New York, NY)*, pages 238–257, 2001. In Hunsaker CT,
686 MF Goodchild, MA Friedl & TJ Case (eds).

- 687 T.W. Simpson, J.D. Poplinski, P.N. Koch, and J.K. Allen. Metamodels for
688 computer-based engineering design: Survey and recommendations. *Engi-
689 neering with Computers*, 17(2), 2001.
- 690 E.R. Stefanescu, M. Bursik, and A.K. Patra. Effect of digital elevation model
691 on geophysical flow model output. *Natural Hazards*, 2010. submitted.
- 692 A.J. Stinton, M.F. Sheridan, A. Patra, K. Dalbey, and L. Namikawa. Incorporation of variable bed friction into TITAN2D mass-flow model: Application to Little Tahoma Peak avalanche (Washington). *Acta Vulcanologica*, 16(1-2):153–163, 2006.
- 696 T. Takahashi and H. Tsujimoto. A mechanical model for Merapi-type pyro-
697 clastic flow. *Journal of Volcanology and Geothermal Research*, 98:91–115,
698 2000.
- 699 K.P. Van Niel, S.W. Laffan, and B.G. Less. Effect of error in the dem on
700 environmental variables for predictive vegetation modelling. *Journal of
701 Vegetation Science*, 15:6:747–756, 2004.
- 702 S. Wechsler and C. Kroll. Quantifying DEM uncertainty and its effects on
703 topographic parameters. *Photogrammetric Engineering & Remote Sensing*,
704 72:108–1090, 2006.
- 705 Q. Weng. Quantifying uncertainty of digital elevation models derived from
706 topographic maps. In: *Advances in Spatial Data Handling*, pages 403–418,
707 2002.

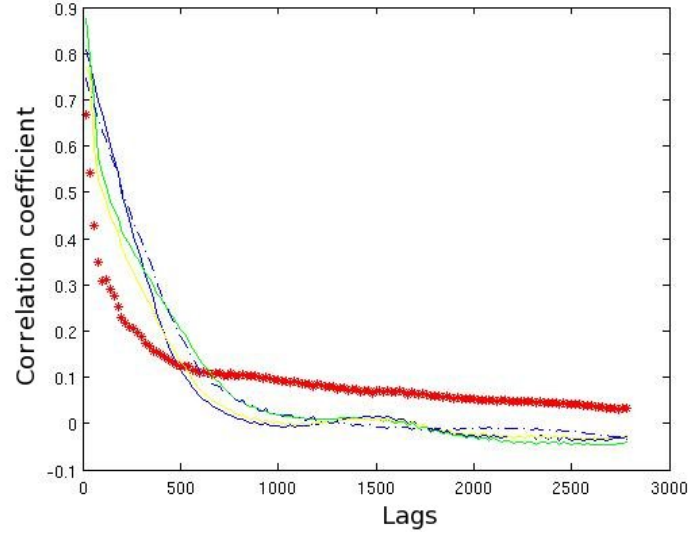
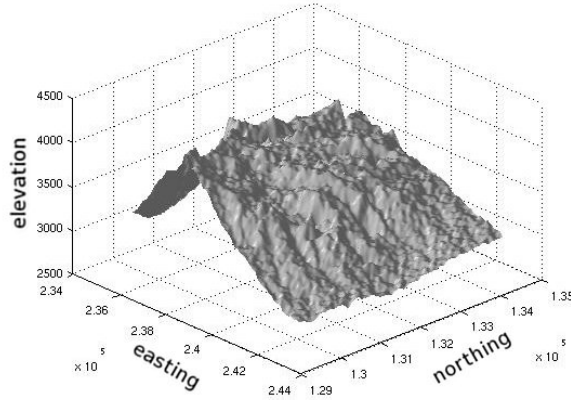
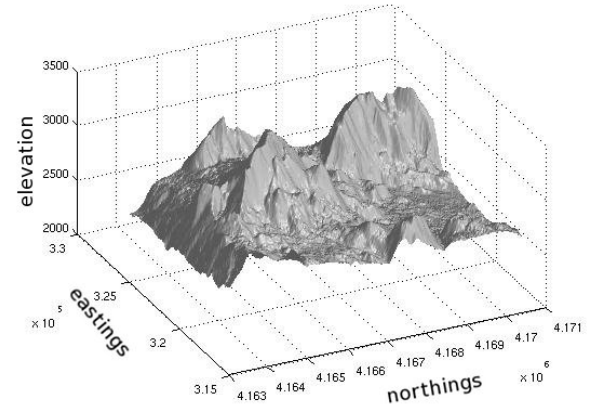


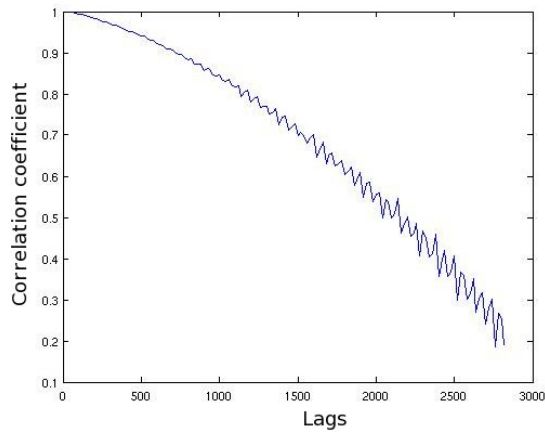
Figure 1: Error map correlogram (red) and various random fields fitted to this by choosing different values for the parameters D, E, F representing the distances of perfect correlation, decay exponent and spatial independence in Equation 2.



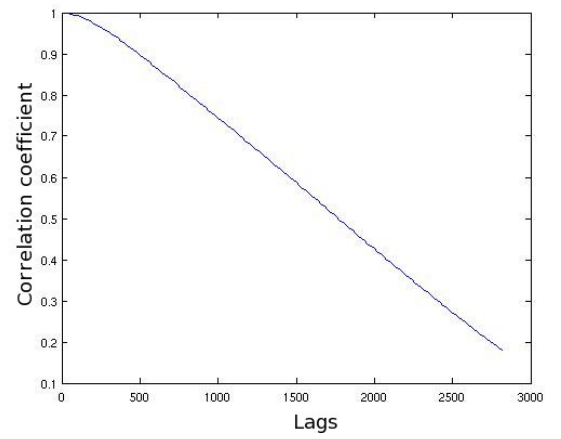
(a)



(b)

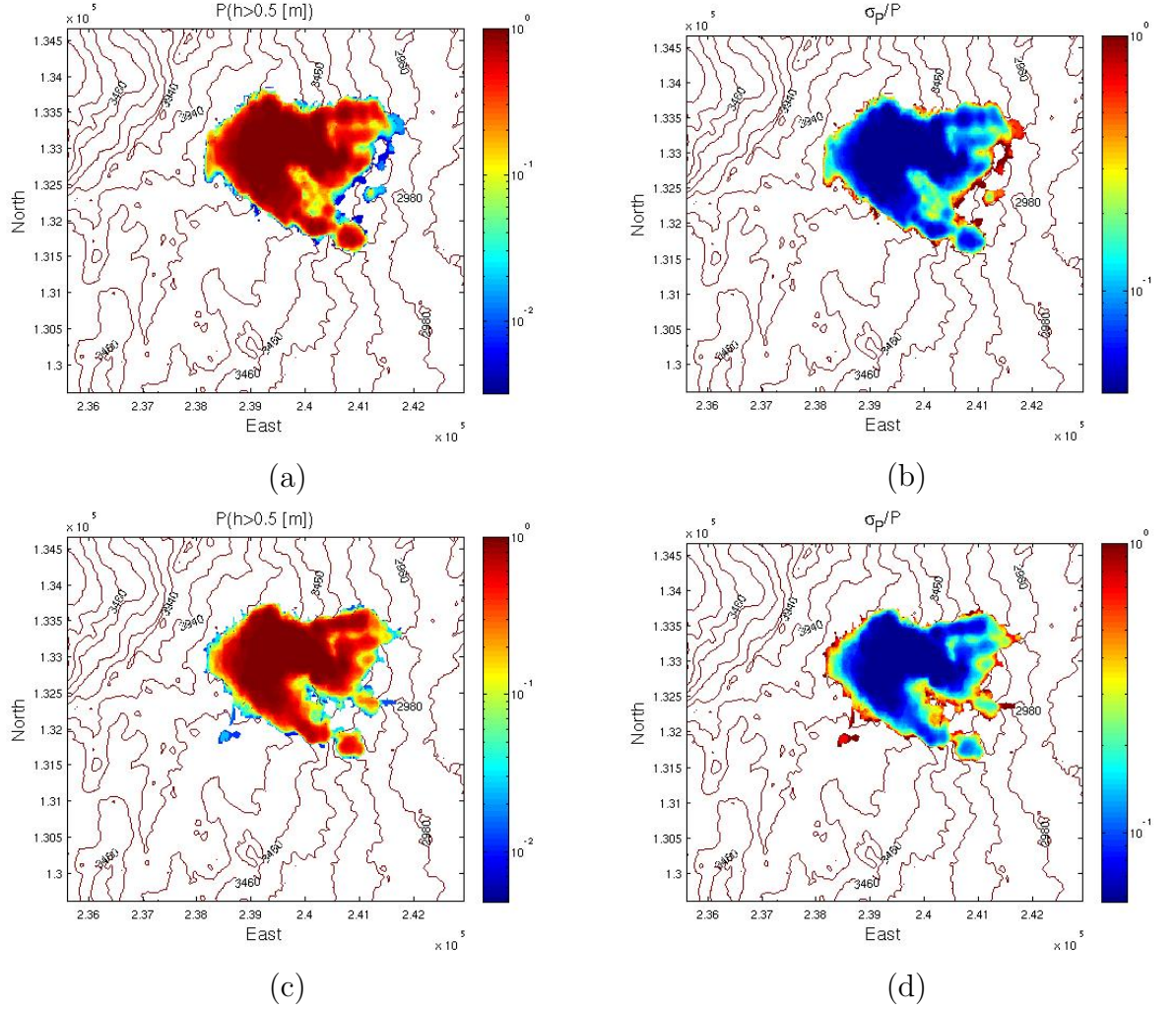


(c)



(d)

Figure 2: a) The Galeras ASTER 30m DEM terrain surface (Easting, Northing and elevation coordinates) (b) The Mammoth NED 30m DEM terrain surface (Easting Northing and elevation coordinates) (c) Galeras Volcano ASTER DEM correlogram (d) Mammoth Mountain TOPSAR DEM correlogram



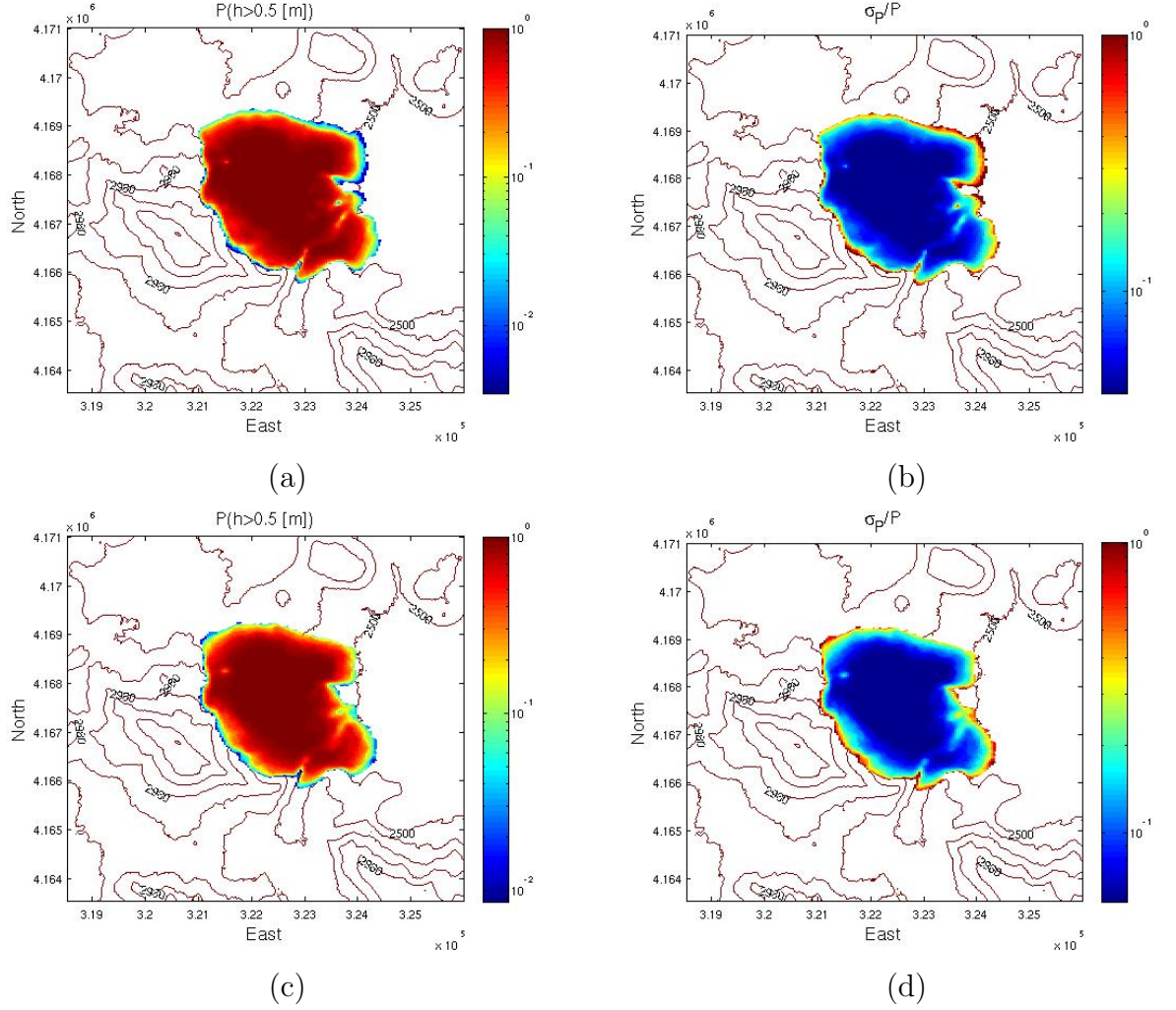
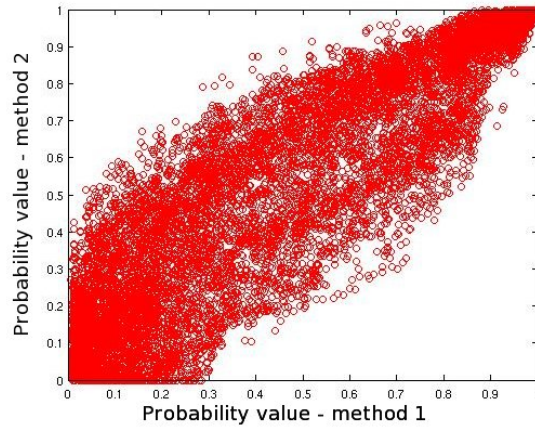
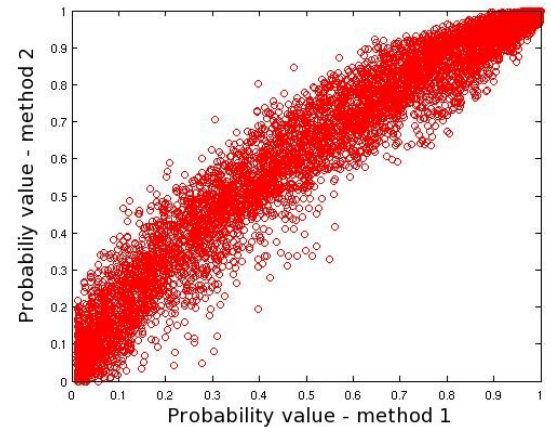


Figure 4: a) Probability that a flow will exceed 0.5 m in depth as a function of position on Mammoth Mountain, CA, given the uncertainties in DEM and input parameters using Method 1 to create DEM realizations. (b) Standard deviation in the estimate that the flow will exceed 0.5 m in depth – Method 1 (c) Probability that a flow will exceed 0.5 m in depth as a function of position on Mammoth Mountain, CA, given the uncertainties in DEM and input parameters using Method 2 to create DEM realizations. (b) Standard deviation in the estimate that the flow will exceed 0.5 m in depth – Method 2

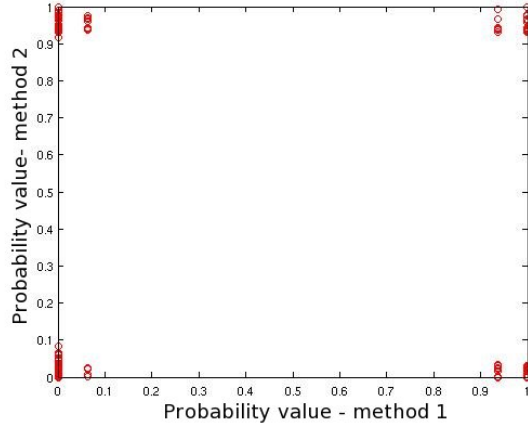


(a)

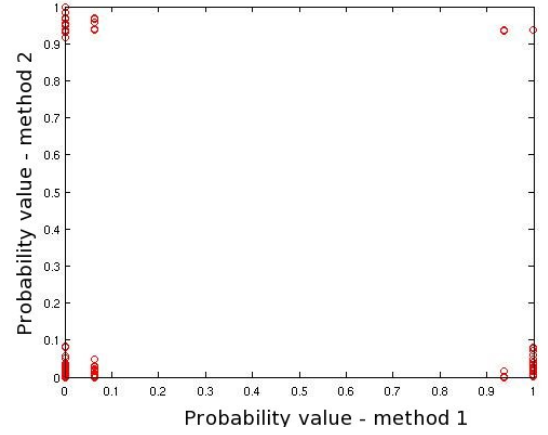


(b)

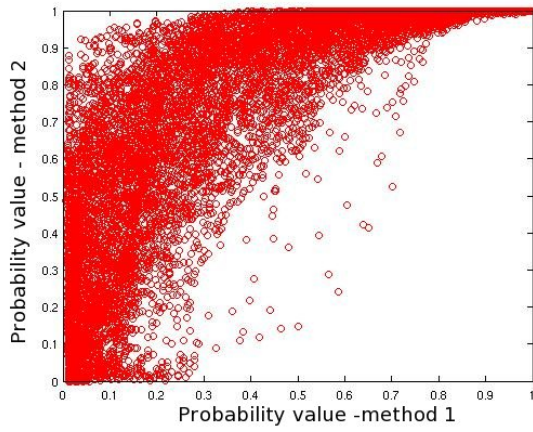
Figure 5: a) The probability that flow will exceed 0.5 m Method 1 versus Method 2 for Galeras Volcano, Colombia (b) The probability that flow will exceed 0.5 m Method 1 versus Method 2 for Mammoth Mountain, CA



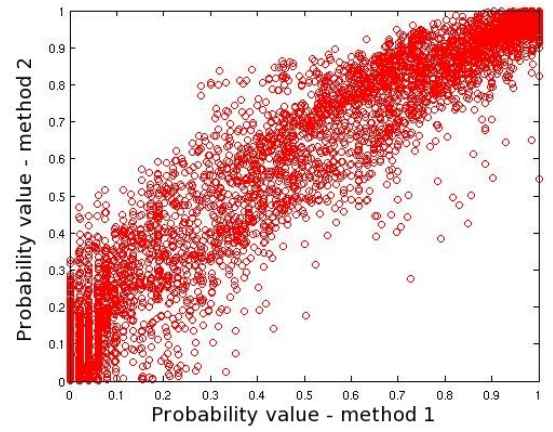
(a)



(b)



(c)



(d)

Figure 6: (a) The probability that flow will exceed 0.5 m Method 1 versus Method 2 for: (a) Galeras Volcano, Colombia for low flow (b) Mammoth Mountain, CA for low flow (c) Galeras Volcano, Colombia for high flow (d) Mammoth Mountain, CA for high flow

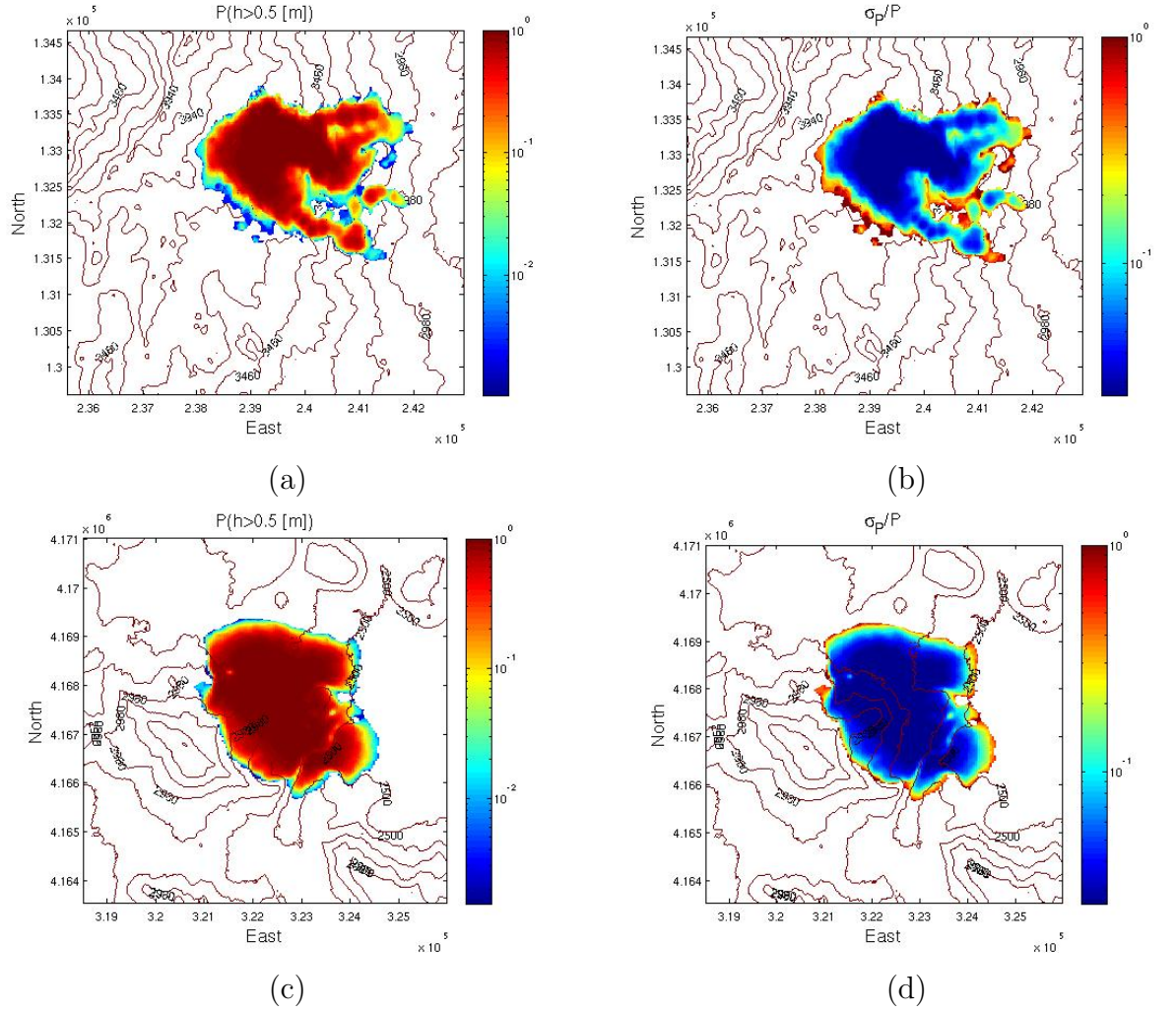
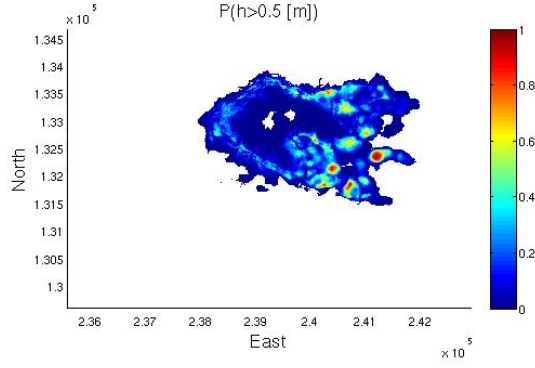
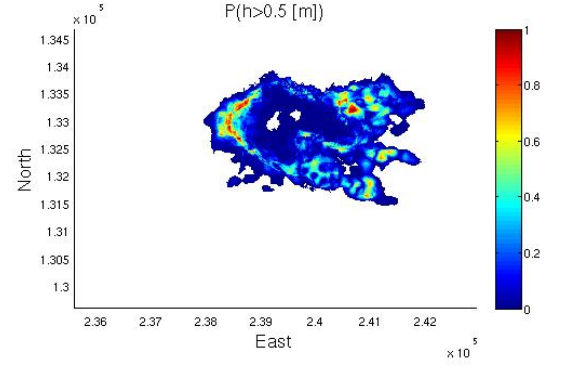


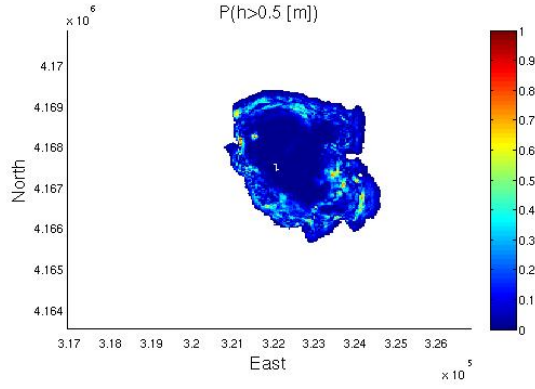
Figure 7: (a) The probability that flow will exceed 0.5 m for Galeras ASTER (b) Standard deviation in the estimate that the flow will exceed 0.5 m in depth for Galeras ASTER (c) The probability that flow will exceed 0.5 m for Mammoth TOPSAR (d) Standard deviation in the estimate that the flow will exceed 0.5 m in depth for Mammoth TOPSAR



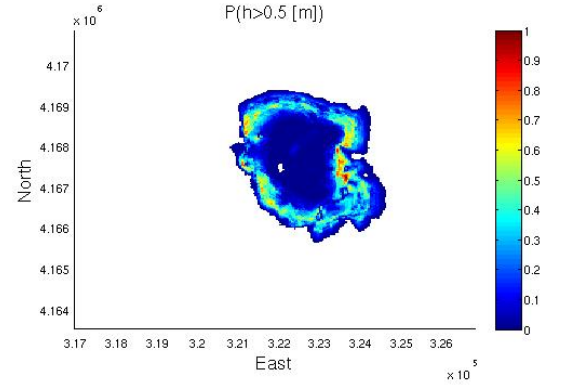
(a)



(b)

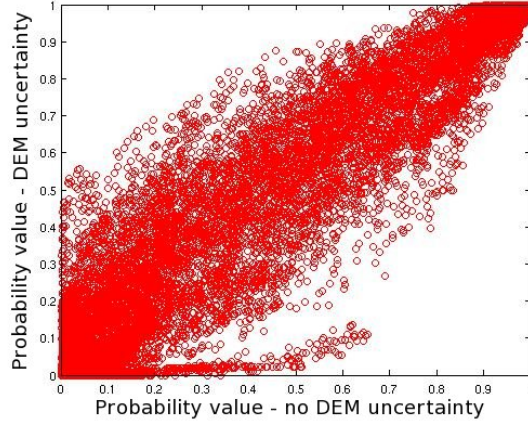


(c)

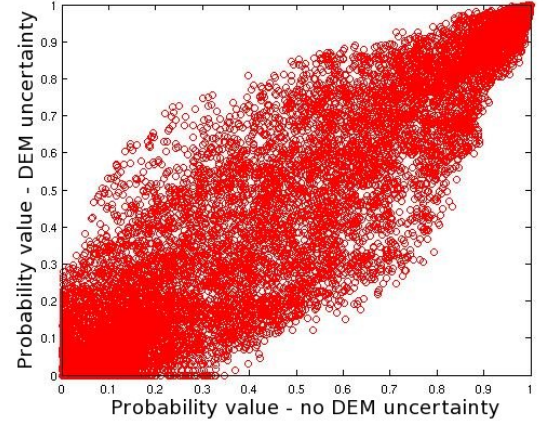


(d)

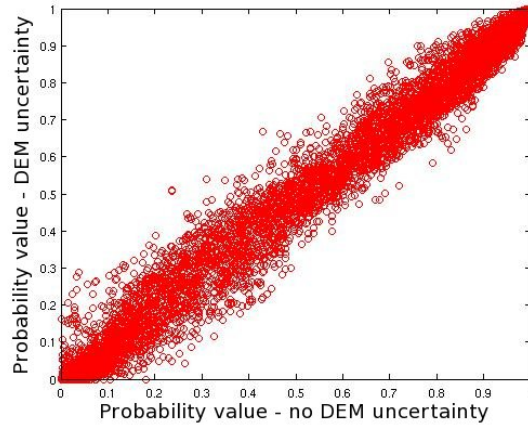
Figure 8: Probability difference map (absolute value) between: (a) Mammoth TOPSAR hazard map and the Method 1 hazard map (b) Mammoth TOPSAR hazard map and the Method 2 hazard map (c) Galeras ASTER hazard map and the Method 1 hazard map (d) Galeras ASTER hazard map and the Method 2 hazard map



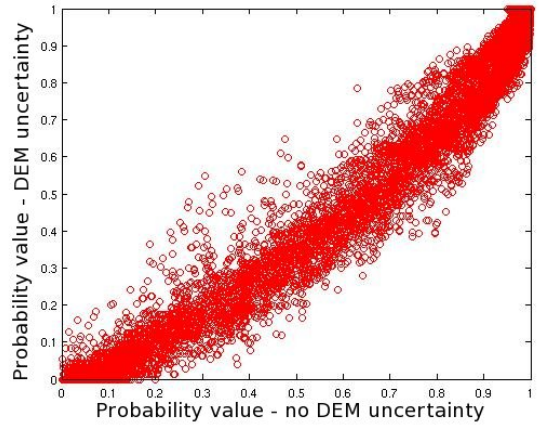
(a)



(b)



(c)



(d)

Figure 9: A comparison of the probability that flow will exceed 0.5 m when we don't assess for the uncertainty in the DEM and when we do, for: (a)Galeras ASTER no DEM uncertainty versus Galeras ASTER DEM uncertainty Method 1 (b)Galeras ASTER no DEM uncertainty versus Galeras ASTER DEM uncertainty Method 2 (c)Mammoth TOPSAR - no DEM uncertainty versus Mammoth TOPSAR - DEM uncertainty Method 1 (d)Mammoth TOPSAR - no DEM uncertainty versus Mammoth TOPSAR - DEM uncertainty Method 2